




Tuning reactivity of Fischer–Tropsch synthesis by regulating TiO_x overlayer over Ru/TiO_2 nanocatalysts

Yaru Zhang^{1,2}, Xiaoli Yang^{1,2,3}, Xiaofeng Yang ^{1✉}, Hongmin Duan¹, Haifeng Qi^{1,2}, Yang Su¹, Binglian Liang¹, Huabing Tao⁴, Bin Liu⁴, De Chen³, Xiong Su ^{1✉}, Yanqiang Huang ^{1✉} & Tao Zhang¹

The activity of Fischer–Tropsch synthesis (FTS) on metal-based nanocatalysts can be greatly promoted by the support of reducible oxides, while the role of support remains elusive. Herein, by varying the reduction condition to regulate the TiO_x overlayer on Ru nanocatalysts, the reactivity of Ru/TiO_2 nanocatalysts can be differentially modulated. The activity in FTS shows a volcano-like trend with increasing reduction temperature from 200 to 600 °C. Such a variation of activity is characterized to be related to the activation of CO on the TiO_x overlayer at Ru/TiO_2 interfaces. Further theoretical calculations suggest that the formation of reduced TiO_x occurs facilely on the Ru surface, and it involves in the catalytic mechanism of FTS to facilitate the CO bond cleavage kinetically. This study provides a deep insight on the mechanism of TiO_x overlayer in FTS, and offers an effective approach to tuning catalytic reactivity of metal nanocatalysts on reducible oxides.

¹State Key Laboratory of Catalysis, Dalian Institute of Chemical Physics, Chinese Academy of Sciences, Dalian 116023, China. ²University of Chinese Academy of Sciences, Beijing 100049, China. ³Department of Chemical Engineering, Norwegian University of Science and Technology, Trondheim 7494, Norway. ⁴School of Chemical and Biomedical Engineering, Nanyang Technological University Singapore, 637459 Singapore, Singapore.
✉email: yangxf2003@dicp.ac.cn; suxiong@dicp.ac.cn; yqhuang@dicp.ac.cn

Fischer–Tropsch synthesis (FTS) offers a powerful way to convert syngas (a mixture of CO and H₂) to long-chain hydrocarbons, by which the transformation of nonpetroleum resources (derived from coal, natural gas, or biomass) into high value-added chemicals and fuels becomes economically efficient and environmentally friendly^{1–3}. The most challenging step in this process is consented as the CO activation, with which the further hydrogenation to CH_x ($x = 1, 2, 3$) species for the carbon chain growth becomes facile on the surfaces of late transition metals like Fe, Co, Ru, and Rh^{4–7}. Among these metals, Ru is identified to be intrinsic of high activity and selectivity in FTS⁸. In particular, large particle sizes of Ru (~8 nm) are highly desirable^{9–11}, on which the direct or H-assisted CO dissociation is greatly facilitated^{12,13}. As such, great efforts have been made on modulating the surface structure of Ru-based catalysts, including by tuning particle size^{9–11}, changing crystal phase¹⁴, and varying exposed plane¹⁵, to further promote the catalytic performance of Ru catalysts.

Beyond that, there are strong metal–support interactions (SMSI) on supported metal catalysts when reducible oxide such as TiO₂ is used as a support^{16,17}. More specifically, reducible oxide migrates to the metal surface by forming a thin overlayer under the reduction condition¹⁸, which then results in a unique metal/support interface and variegates the behavior of catalyst in reactions^{19–21}. The utilization of such SMSI has also been demonstrated to be an alternative strategy to enhance the catalytic reactivity of metal catalysts in FTS^{22,23}. This promoted effect is generally attributed to the interface between metal and support, which serves as a new active site with an improved activity in the reactions^{18,23}. However, the catalytic mechanism and the intrinsic roles of such newly generated interfaces are remaining elusive.

In this research, by regulating a TiO_x overlayer on the Ru nanoparticles (~2 nm), the catalytic activity of this Ru/TiO₂ nanocatalyst in FTS can be boosted. With various characterizations and theoretical modeling, the reduced TiO_x overlayer on Ru nanocatalysts is demonstrated to participate in and dramatically facilitate the bond cleavage of CO. The results of this work are expected to play an important role in the mechanism understanding of SMSI in FTS, and also provide guidance with regard to tuning the catalytic properties of metal nanocatalysts supported on reducible oxides.

Results

Structural characterization. With the aim to investigate the effect of TiO_x overlayer covered over the Ru nanoparticles (NPs) on the reactivity in FTS, in the present work, we use wet impregnation method to fabricate Ru-based catalysts with small-sized metal nanoparticles by using rutile TiO₂ as a support²⁴. In this text, catalysts reduced at specific temperatures were denoted as Ru/TiO_{2-x}, where x refers to reduction temperatures ($x = 200–600$). The loading of Ru, after calcination in air and the following thorough chlorides removal process, has been determined to be 2.2 wt% by ICP-OES. As indicated by Brunauer–Emmett–Teller (BET) testing (Supplementary Table 1), different Ru/TiO_{2-x} samples are similar in physical textures, with almost the identical surface areas and pore volumes.

Meanwhile, all Ru/TiO₂ samples are found to possess analogous morphologies of metal NPs, that is, the Ru NPs are all well dispersed on the support and have a uniform size distribution with an average diameter of ~2 nm (Fig. 1a, b and Supplementary Figs. 1–3). It was attributed to the usage of rutile TiO₂ as the support in our research, which possesses the same crystal phase and comparable lattice parameters with that of RuO₂ (Supplementary Table 2). As a result, the calcination step by formation of RuO₂/TiO₂ interphase helps to resist the aggregation of metal nanoparticles even after the high-temperature pretreatment (Supplementary Fig. 4). On the other hand, however, there are significant discrepancies on the micro-structures of Ru NPs on the TiO₂ support when pretreated at different reduction temperatures (Fig. 1c and Supplementary Fig. 5). In detail, a distinct morphology of Ru NP can be resolved on the support when sample was reduced at a temperature below 300 °C, while a visible coating on the Ru NPs can be distinguishable after higher temperature pre-reduction. In terms of the SMSI between Ru and rutile TiO₂, it was ascribed to the TiO_x overlayer over the Ru NPs under high-temperature reduction condition, and the migration of TiO_x over Ru NPs was initiated at a reduction temperature higher than 300 °C.

To get a qualitative comparison of the exposure of Ru species after coating by TiO_x overlayer, the chemisorption of CO and H₂ were measured to estimate the Ru dispersion on these Ru/TiO_{2-x} samples. As seen in Table 1, the values obtained by different probe molecules give the same tendency of the metal dispersions

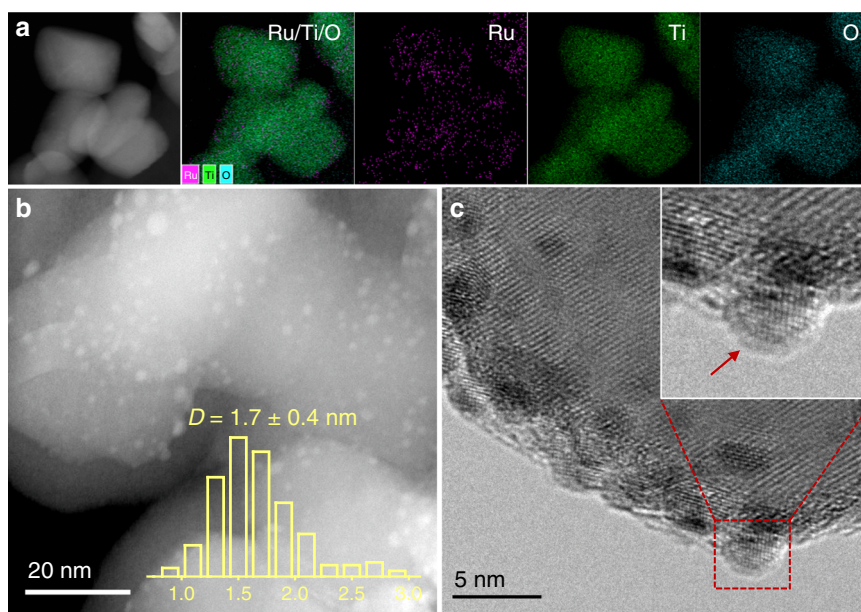


Fig. 1 Morphological study of the Ru/TiO₂ catalysts. **a** Elemental mapping of Ru/Ti/O in the fresh Ru/TiO₂ catalyst. **b** HAADF-STEM image of the Ru/TiO₂ catalyst pretreated at 600 °C (Ru/TiO₂-600 sample) with the metal size distribution. **c** HRTEM image of the Ru/TiO₂-600 catalyst.

for different Ru/TiO_{2-x} samples, that is, the dispersion of Ru decreases with increasing the reduction temperature from 300 to 600 °C. This can be explained by a gradual encapsulation of the Ru NPs by TiO_x overlayer as increasing the reduction temperature from 300 to 600 °C, which was in good agreement with the TEM observations. As compared, the dispersion derived from H₂ chemisorption was lower than that from CO chemisorption. It might be caused by the Ruⁿ⁺ sites at the Ru-TiO₂ interface, which are unavailable for H₂ chemisorption due to the SMSI effects²⁵, but it can be readily involved in CO chemisorption as indicated in our further in situ DRIFT spectra experiments. Even so, the H₂ uptakes on the Ru/TiO₂-200 sample was found to be less than that of the Ru/TiO₂-300. This can be explained by the results of H₂ temperature-programmed reduction (H₂-TPR), in which the predominant reduction of Ru/TiO₂ to metallic Ru occurring at a temperature higher than 200 °C (Supplementary Fig. 6). In addition, the decline of the surface metallic Ru exposure by a gradual encapsulation of the Ru NPs by TiO_x overlayer as increasing the reduction temperature was also confirmed by the underpotential deposition of copper (Cu upd) experiments, with which the metallic surface area can be semi-quantified in terms of the integral area of current for the reduction deposition of copper on the exposed metal surface²⁶ (Supplementary Fig. 7 and Supplementary Table 3).

The evolution of Ru/TiO₂ catalysts at different temperature reductions was also investigated with X-ray absorption spectroscopy (XAS). The extended X-ray absorption fine structure (EXAFS) of Ru *K*-edge and the fitting results (Fig. 2a and Supplementary Table 4) have demonstrated that the coordination number (CN) associated with Ru-Ru pair (~2.67 Å) is increased

gradually from 2.2 to 5.3 as the reduction temperature increased from 200 to 600 °C, while the CN of the Ru-O pair (~1.98 Å) presents an inverse tendency by decreasing from 4.0 to 2.4. It suggests a gradual improvement of the reduction degree of ruthenium oxide to metallic phase. Correspondingly, a shift of edge energy towards Ru foil was observed by the X-ray absorption near-edge structure (XANES) (Supplementary Fig. 8). Nevertheless, the inevitable Ru-O bonding for Ru/TiO₂ samples indicates a strong interfacial interaction between Ru and TiO₂, further confirming the formation of TiO_x coating on the Ru NPs. On the other hand, the soft XANES spectra at the Ti *L*_{3,2}-edge (Fig. 2b) exhibit a decline in peak intensities with the increase of pretreatment temperature, indicative of an increasing degree of the reduction of TiO₂, owing to the formation of TiO_x overlayer on Ru NPs. The growth of the reduced TiO_x overlayer was also evidenced by the increased concentration of Ti³⁺ species accompanying by the decreased ratio of surface Ru/Ti estimated from the Ti-2*p* and Ru-3*p* in XPS results (Supplementary Fig. 9 and Supplementary Table 5).

On the basis of the above observations, the structure evolution of Ru/TiO₂ at different stages of reduction was then suggested in Fig. 2c. Benefiting from the lattice matching of RuO₂/TiO₂ interphase, a small size of Ru NPs with the improved sintering resistance can be readily acquired by the following reduction pretreatment. In the initial step of reduction, e.g., Ru/TiO₂-300, a dominant metallic Ru will be exposed, and it serves as a typical Ru-based nanocatalysts in FTS. With further increasing the reduction temperature, the SMSI between Ru and TiO₂ governs the surface exposure of Ru NPs, and the TiO_x thin layer begins to migrate and coating the Ru surface, resulting in a shrinkage of

Table 1 H₂ and CO chemisorption results for different Ru/TiO_{2-x} samples.

Sample	CO uptake (μmol _{CO} g _{Ru} ⁻¹)	Ru dispersion by CO uptake	H ₂ uptake (μmol _{H2} g _{Ru} ⁻¹)	Ru dispersion by H ₂ uptake
Ru/TiO ₂ -200	102.6	47.2%	28.1	25.8%
Ru/TiO ₂ -300	94.2	43.3%	32.2	29.6%
Ru/TiO ₂ -400	84.7	38.9%	27.5	25.3%
Ru/TiO ₂ -450	74.0	34.0%	21.6	19.9%
Ru/TiO ₂ -500	59.8	27.5%	17.4	16.0%
Ru/TiO ₂ -600	38.0	17.5%	10.8	9.9%

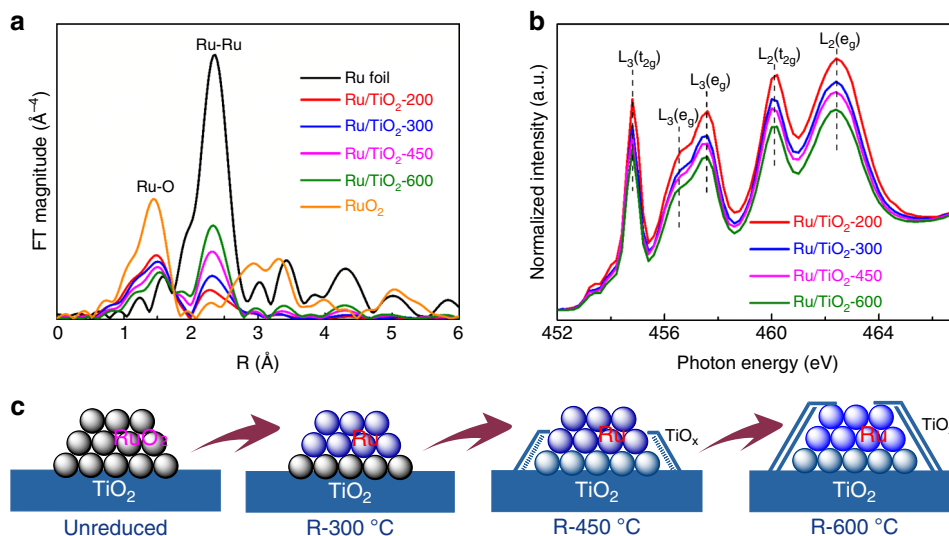


Fig. 2 The evolution of Ru/TiO₂ catalysts reduced at different temperatures. **a** Fourier transforms of the *k*³-weighted EXAFS of Ru *K*-edge for Ru foil, RuO₂, and the Ru/TiO₂ catalysts pretreated at different temperatures (Ru/TiO_{2-x} samples). **b** Ti *L*_{3,2}-edge XANES for the Ru/TiO₂ catalysts pretreated at different temperatures (Ru/TiO_{2-x} samples). **c** A schematic illustration of the structural evolution of Ru/TiO₂ at different stages of reduction.

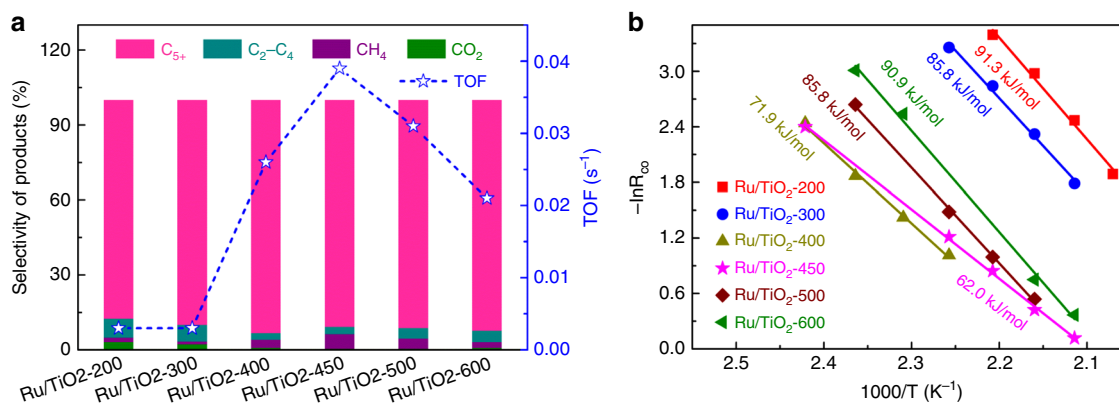


Fig. 3 Catalytic results of the Ru/TiO₂ catalysts for Fischer-Tropsch synthesis. **a** Catalytic performance of the Ru/TiO₂ catalysts pretreated at different temperatures (Ru/TiO₂-x samples). Reaction conditions: 2 MPa, 160 °C, space velocity = 1200–6000 mL h⁻¹ g_{cat}⁻¹, H₂/CO/Ar = 64/32/4. **b** Arrhenius plots for CO hydrogenation over the Ru/TiO₂-x catalysts.

metallic Ru surface by the TiO_x overlayer (like that on Ru/TiO₂-450). Finally, for the Ru/TiO₂-600 sample, an excessive coverage of TiO_x on Ru NPs causes a dominant TiO_x overlayer on Ru nanocatalysts. Accordingly, a tunable degree of TiO_x overlayer on Ru NPs can be easily achieved by varying the pretreatment condition, and it thus provides us an opportunity to explore the effect of metal/support interface of Ru/TiO₂ on the activity in FTS.

Catalytic performance. The catalytic performances of various Ru/TiO₂-x catalysts in FTS were then evaluated at 160 °C with a 2 MPa reaction pressure according to our preliminary optimization of experiment conditions for achieving a high C₅₊ selectivity under a relatively mild condition (Supplementary Fig. 10). Notably, as shown in Fig. 3a and Supplementary Figs. 11, 12, all Ru/TiO₂-x catalysts possess an excellent C₅₊ selectivity with a value up to 90%, indicating the promising application prospect of Ru/TiO₂ in FTS for high-carbon products. While the intrinsic reaction rate (reflected as the TOF value) greatly relies on the pretreatment temperature, and shows a volcano-like trend with the increase of reduction temperature (Fig. 3a, Supplementary Fig. 13 and Supplementary Table 6). As compared, samples of Ru/TiO₂-200 and Ru/TiO₂-300 manifest a much lower intrinsic activity (0.003 s⁻¹). A great promotion of activity was observed for the Ru/TiO₂-400 catalyst. Among these catalysts, the Ru/TiO₂-450 exhibits the highest activity with an intrinsic TOF value of 0.039 s⁻¹, which was also superior to other Ru-based catalysts reported previously (Supplementary Table 7). The further increasing of pretreatment temperature, however, causes an activity decay of catalysts, with a TOF value of only 0.021 s⁻¹ for Ru/TiO₂-600. Correspondingly, a reverse variation of apparent activation energy (E_a) was obtained, i.e., the Ru/TiO₂-450 presents the lowest E_a with a calculated value of 62.0 kJ mol⁻¹, which was much lower than the values of other Ru/TiO₂ catalysts (Fig. 3b).

The particle size of metal was essential in determining the performance of Ru-based catalysts in FTS. The activity increases as the particle size of Ru nanocatalyst increased, with the small-sized Ru NPs behaving a rather poor activity^{9–11}. This explains well the low activity of our small-sized Ru/TiO₂ catalysts reduced at low temperatures (Ru/TiO₂-200 and Ru/TiO₂-300 samples) as well as Ru NPs supported on the irreducible support (Ru/Al₂O₃-450 in Supplementary Fig. 14 and Supplementary Table 8). While an enhanced activity of Ru/TiO₂-450 catalyst suggests that the TiO_x overlayer on Ru NPs has a positive contribution on the reactivity of Ru nanocatalysts. However, in terms of the decline of

activity for the Ru/TiO₂-600 catalyst covered dominantly by TiO_x overlayer, the only TiO_x overlayer cannot achieve a high activity for the FTS reaction. In this regard, the interface between metal and support of Ru/TiO₂ plays a crucial role on the activity promotion, where both the metallic Ru and TiO_x overlayer are indispensable. The optimized composition of TiO_x overlayer and Ru NPs on Ru/TiO₂-450 catalyst makes it possess an enhanced activity.

Furthermore, the Ru/TiO₂-450 catalyst also owns an excellent stability in the steady running state of FTS (Supplementary Figs. 10, 11). HAADF-STEM image of the spent Ru/TiO₂-450 catalyst suggests that the size of Ru can keep constant after testing (Supplementary Fig. 15). This was also benefited from the SMSI in the Ru/TiO₂-450 catalyst, which greatly prohibits the size aggregation of Ru during FTS process.

Catalytic mechanism. The role of the TiO_x overlayer was then studied by the steady-state isotopic transient kinetic analysis (SSITKA)^{27,28}, by which the evolution of intermediates with the associated coverage and reactivity can be acquired (Supplementary Fig. 16). Limited by the atmospheric pressure condition in this analysis, as shown in Supplementary Fig. 17, CH₄ selectivity has an increase because of the preference of hydrogenation over C–C coupling for CH_x intermediates. Notably, a good correlation between the intrinsic activity (TOF) of CO consumption and methane generation can be set up. As such, the coverage of CH_x (represented as θ_{CH₄} in SSITKA) was determined as a function of reduction temperature of Ru/TiO₂ (Fig. 4a). From our results, the activity improvement of Ru/TiO₂-450 can be attributed to the increased coverage of CH_x intermediates on the catalyst surface²⁹. By considering the comparable size of Ru for different Ru/TiO₂ samples, a promoted effect toward CO activation to generate CH_x intermediates with the aid of TiO_x overlayer can be expected on the Ru/TiO₂-450 catalyst.

To confirm our proposed mechanism of CO activation, the micro-calorimetry toward CO was measured for Ru/TiO₂ samples (Fig. 4b, c). The amount of CO chemisorption follows a trend of Ru/TiO₂-300 > Ru/TiO₂-450 > Ru/TiO₂-600. This can be explained by the decrease exposure of Ru for serving as the adsorbed sites toward CO as increasing reduction temperature. In particular, as compared with other catalysts, Ru/TiO₂-450 owns a large portion of CO chemisorption at a relative higher differential heat (>150 kJ mol⁻¹). This was attributed to the CO chemisorption on the interface site, followed by a dissociation of CO with the aid of TiO_x overlayer. For comparison, the Ru/TiO₂-300 shows a predominant moderate chemisorption toward CO, with a

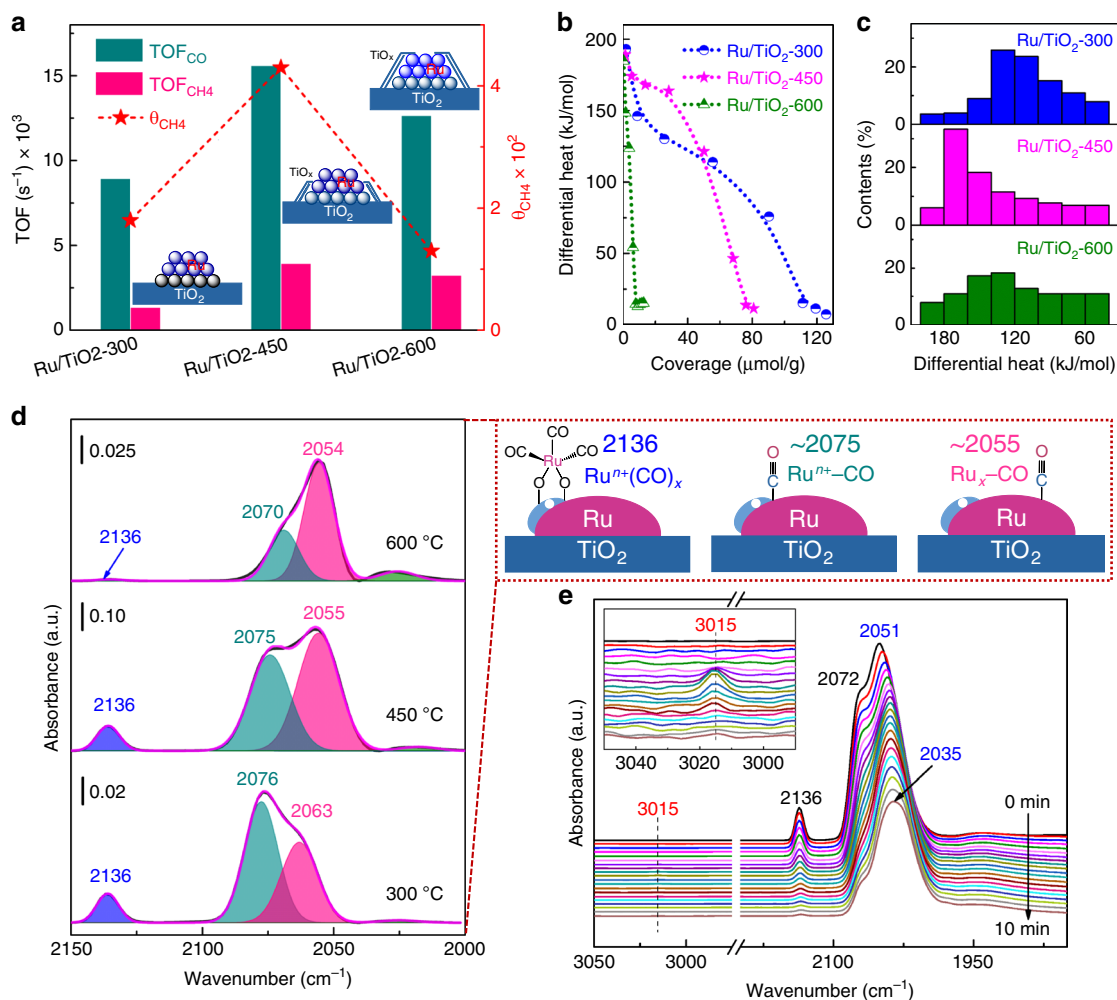


Fig. 4 The participation of the TiO_x overlayer in the C–O bond dissociation. **a** The correlation between the intrinsic activity (TOF_{CO} and TOF_{CH₄}) and the coverage of active surface CH_x intermediates (represented by θ_{CH_4}) as obtained by SSITKA experiments. Performing condition: 200 °C, 0.185 MPa, H₂/CO = 10. **b, c** Microcalorimetric measures of CO chemisorption and the distribution of differential heat on the Ru/TiO₂-*x* samples. **d** In situ DRIFT spectra obtained after CO adsorption and evacuation with helium at 160 °C, over the Ru/TiO₂-*x* catalysts. **e** Evolution of the CO_{ad} species during H₂ flow at 160 °C as determined using in situ DRIFT spectra, over the Ru/TiO₂-450 catalyst.

differential heat of 120–150 kJ mol⁻¹ for CO chemisorption on the Ru sites. In contrast, the over-coverage of TiO_x on Ru NPs causes a shortage of both the Ru sites and the interfaces for CO chemisorption/dissociation on Ru/TiO₂-600.

In situ diffuse reflectance infrared Fourier transform (DRIFT) spectra of CO chemisorption on Ru/TiO₂-*x* indicate that there are three distinct ν_{CO} bands located at approximately 2136, 2075, and 2056 cm⁻¹ in the carbonyl region (Fig. 4d). Here, the bands at 2136 and 2075 cm⁻¹ were often observed by performing CO adsorption on well-dispersed, partially oxidized Ruⁿ⁺ with a low coordination environment, which therefore were ascribed to multi-carbonyl (Ruⁿ⁺(CO)_x) and mono-carbonyl (Ruⁿ⁺-CO) species adsorbed on partially oxidized Ruⁿ⁺ sites on the interface, respectively^{30–32}. While the peak at 2056 cm⁻¹ was assigned to linear CO adsorption on metallic Ru (Ru_x-CO)^{33,34}. After purging H₂ into the CO-saturated Ru/TiO₂, the gaseous CH₄ product with a characterized frequency at 3015 cm⁻¹ was detected³⁵, accompanying by the consumption of CO (Fig. 4e and Supplementary Fig. 18). More importantly, by the complete consumption of CO of Ruⁿ⁺(CO)_x and Ruⁿ⁺-CO, the further conversion of CO was restrained, with Ru_x-CO as a predominant chemisorption species on Ru surface. In this case, the interface of partially oxidized Ruⁿ⁺ sites were supposed to be the active sites

for the FTS reaction. As such, the intensity of CO related to FTS on the Ru/TiO₂-450 was found to be more remarkable than that of Ru/TiO₂-300 and the Ru/TiO₂-600 catalysts (Fig. 4d), which was responsible for its higher activity in FTS.

According to our results, a catalytic mechanism for CO transformation on the Ru/TiO₂-*x* catalysts was then proposed. Due to the SMSI over Ru/TiO₂, the TiO_x overlayer on Ru NPs provides oxygen vacancies for anchoring the oxygen atoms from the dissociation of carbonyl group; it thus greatly facilitates the dissociation of CO on the Ru/TiO_x interface of catalysts as also suggested by Bell and coworkers³⁶, by which the hydrogenation and C–C coupling can be realized on the Ru sites to produce carbon chain products. As for Ru/TiO₂-450, the optimized TiO_x overlayer on Ru NP offers it a maximized activity in FTS, while the shortage of interface on both the Ru/TiO₂-300 and Ru/TiO₂-600 samples leads to a lower activity in FTS. As such, the participation of the TiO_x overlayer in the C–O bond dissociation process was responsible for the superior reactivity of the Ru/TiO₂-450 catalyst.

DFT calculations. Theoretically, we have performed a density functional theory (DFT) study on the CO activation on the model catalyst on a TiO_x cluster decorated Ru(001) surface. In Fig. 5a

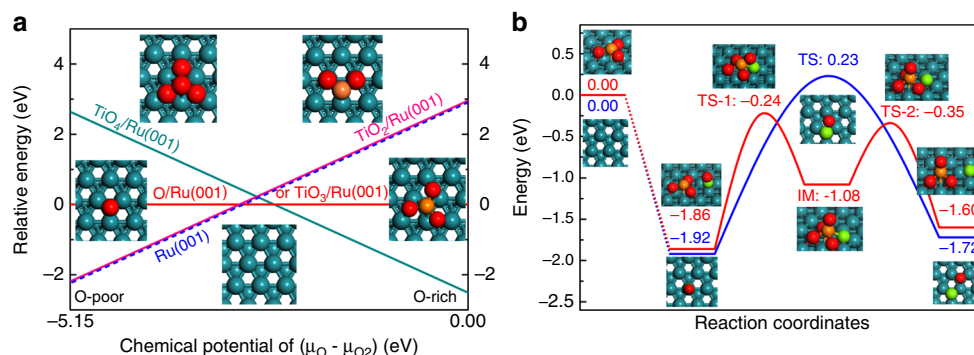


Fig. 5 Theoretical study of the CO activation on a TiO_x cluster decorated $\text{Ru}(001)$ surface. **a** Thermodynamic stability of different $\text{TiO}_x/\text{Ru}(001)$ and $\text{O}/\text{Ru}(001)$ under a variation of the chemical potential of O as referring to $\text{TiO}_3/\text{Ru}(001)$ and $\text{Ru}(001)$, respectively, with the atomic configuration in insets. Atom key: Ru (dark blue), O (red), Ti (orange), and C (green). **b** A possible catalytic mechanism of CO activation at GW level calculations on the $\text{TiO}_3/\text{Ru}(001)$ model surface (red line), with the dissociation of CO on $\text{Ru}(001)$ surface as a comparison (blue line).

and Supplementary Table 9, we have first studied the thermodynamic stability of different TiO_x clusters on the $\text{Ru}(001)$ surface at different oxygen chemical potential. As compared with the TiO_6 unit in bulk phase of rutile TiO_2 , the TiO_x was reduced facilely on the $\text{Ru}(001)$ surface, and the TiO_4 cluster was found to be dominant under the oxygen-rich condition. By decreasing the oxygen chemical potential under reduction condition, the reduction of TiO_4 occurred readily on the Ru surface through a sequential reduction to $\text{TiO}_3/\text{Ru}(001)$ and $\text{TiO}_2/\text{Ru}(001)$, respectively. This was consistent with the experimental observation of a reduction of the TiO_x overlayer under the reduction condition. On the $\text{TiO}_3/\text{Ru}(001)$ surface, the activation of CO by C–O bond cleavage was then estimated, with that occurring on parent $\text{Ru}(001)$ surface as a comparison. As we can see in Fig. 5b, the CO bond cleavage on the $\text{Ru}(001)$ surface has a much high barrier (2.15 eV), and the laying down of the atop $^*\text{CO}$ adspecies adsorbed on the surface is the main obstacle during its dissociation, in good agreement with the previous results^{37,38}. In contrast, with a reduced TiO_3 cluster decorating on the $\text{Ru}(001)$ surface, the bond cleavage of CO adsorbed on the Ru site of interface can be greatly promoted by experiencing a calculated barrier of 1.62 eV, with the aid of TiO_3 as the O seizer of carbonyl group to transform to TiO_4 . Taking into account that our experiments of FTS were conducted at a reaction temperature of 160–200 °C and a reaction pressure of 2 MPa, such a barrier is facile to overcome on the Ru/TiO_2 catalysts at the reaction condition of FTS. The as-dissociated C^* adspecies can then be conveniently diffused from the $\text{TiO}_x/\text{Ru}(001)$ interface to $\text{Ru}(001)$ (0.73 eV) for the further hydrogenation. Meanwhile, the reduction of $\text{TiO}_4/\text{Ru}(001)$ to $\text{TiO}_3/\text{Ru}(001)$ was even thermodynamically more favorable than the surface reduction of O adspecies on the parent $\text{Ru}(001)$ surface (Fig. 5a), which can then facilitate the catalytic cycle of CO activation on the interface. As indicated by the previous reports, such C^* species is promising to be hydrogenated to CH_x species and realize the C–C coupling on the Ru surface to produce the C_{2+} products³⁹. Accordingly, the Ru/TiO_2 -450 catalyst, owing to its optimized Ru/TiO_x interface for CO activation, shows a superior activity to other Ru/TiO_2 - x catalysts in FTS.

In conclusion, we have successfully fabricated a highly active Ru/TiO_2 catalyst for FTS by fine-tuning the catalyst pre-reduction condition. With increasing the reduction temperature, the TiO_x overlayer is gradually enveloping the Ru NPs. The catalyst reduced at 450 °C exhibits a high intrinsic activity under mild conditions with a low apparent activation energy. The participation of TiO_x overlayer in promoting CO dissociation plays a vital role in activity enhancement during FTS. An optimized TiO_x

overlayer on the Ru NPs formed during reduction at 450 °C is evidently able to capture oxygen from carbonyl group adsorbed on the interface of Ru/TiO_x . This, in turn, facilitates the cleavage of C–O bonds. This work not only provides an understanding of the mechanism of CO activation on Ru/TiO_2 catalysts, but also suggests an effective approach to tailoring the catalytic properties of metal nanocatalysts supported on reducible oxides.

Methods

Catalyst preparation. The Ru/TiO_2 catalysts were prepared by an impregnation method using rutile TiO_2 as the support. In a typical synthesis, 1.6 g of the aqueous $\text{RuCl}_3 \cdot 3\text{H}_2\text{O}$ solution (8.2 wt%, 0.0317 g Ru per gram of solution, AR) was diluted to 30 mL with deionized water. 2.0 g of rutile TiO_2 (40 nm, 99.8% metal basis) was then added to the solution and the resulting suspension was evaporated to dry in a 50 °C water bath with the vigorous stirring. The resulting solid was dried at 120 °C overnight, followed by the calcination in air at 300 °C for 3 h. Subsequently, to remove the residual chlorides, the sample was washed repeatedly with a dilute ammonia solution (1 mol L⁻¹), followed by filtrating and washing with deionized water until there was no more precipitate in the filtrate detected by AgNO_3 solution (0.1 mol L⁻¹). Finally, the sample was dried at 60 °C overnight. The sample thus obtained was denoted as the fresh Ru/TiO_2 . Prior to catalytic performance tests, the fresh Ru/TiO_2 sample were reduced in situ under a H_2 gas flow (20 mL min⁻¹) at specific temperatures. The samples after reduction were denoted as Ru/TiO_2 - x , where x indicates the reduction temperature (200, 300, 400, 450, 500, or 600 °C). The Ru loading in the Ru/TiO_2 catalyst is 2.2 wt% as detected by ICP-OES.

Catalyst characterization. High-angle annular dark field scanning transmission electron microscopy (HAADF-STEM) together with the elemental mapping and high-resolution transmission electron microscopy (HRTEM) images were acquired using a JEOL JEM-2100F microscope operating at 200 kV. The Ru particle size was determined from HAADF-STEM images, and at least 200 particles were counted for each sample. The Ru concentrations in specimens were determined by inductively coupled plasma optical emission spectroscopy (ICP-OES) with an ICP-OES 7300DV instrument.

CO and H_2 chemisorption experiments. The exposure of Ru species after coating by TiO_x was determined by CO and H_2 pulse chemisorption on a Micromeritics AutoChem II 2920 instrument. For CO (or H_2) chemisorption experiment, the sample (~100 mg) was pretreated with hydrogen at desired temperatures for 1 h, followed by purging with high-purity helium (or argon) for 30 min. After the sample was cooled down to 50 °C, a 5% CO/He (or 10% H_2 /Ar) mixture was injected into the reactor repeatedly until CO (or H_2) adsorption was saturated. The dispersion of Ru was calculated from the amount of CO (or H_2) adsorbed by assuming the CO/Ru (or H/Ru) adsorption stoichiometry to be 1/1.

X-ray absorption spectroscopy. Pseudo-in situ X-ray absorption spectroscopy (XAS), including acquiring X-ray absorption near-edge structure (XANES) and extended X-ray absorption fine structure (EXAFS) data at the Ru K-edge, was performed at the BL 14W1 of Shanghai Synchrotron Radiation Facility (SSRF), China. A double Si (311) crystal monochromator was used for energy selection. The samples were pretreated in a H_2 flow (20 mL min⁻¹) at the desired temperatures for 2 h, followed by sealing with Capton film in a glove box without exposure to air. The spectra were collected at room temperature in the transition mode. The Ti L_{3,2}-edge XANES data was acquired at the XMCD beamline (BL12B)

at the National Synchrotron Radiation Laboratory (NSRL), China. The Athena software package was used to analyze the data.

CO microcalorimetric measurements. The differential heat of CO adsorption was measured for each specimen at 40 °C using a BT 2.15 Calvet calorimeter connected to gas handling and volumetric systems equipped with MKS 698A Baratron capacitance manometers ($\pm 1.33 \times 10^{-2}$ Pa). Previous to CO adsorption, the samples were treated in a H₂ flow at the desired temperatures for 1 h, followed by evacuation for 30 min at the same temperature. After cooling to room temperature in vacuum, the quartz tube was refilled with He and tightly sealed, after which the samples were outgassed at 40 °C overnight in the calorimetric cell. CO adsorption was carried out during the stepwise introduction of pure CO up to a pressure of ~ 10 Torr at 40 °C.

In situ DRIFTS. In situ diffuse reflectance infrared Fourier transform (DRIFT) spectra were acquired using a Bruker Equinox 55 spectrometer equipped with a mercury cadmium telluride (MCT) detector, recorded with a resolution of 4 cm⁻¹. Prior to CO adsorption, the samples were treated in situ in the DRIFT cell under a H₂ flow (20 mL min⁻¹) at the desired temperatures for 1 h, followed by purging with a He flow at the same temperature for 30 min. After cooling to 160 °C, a background spectrum was collected, following which the He flow was switched to a 5 vol% CO in He flow (20 mL min⁻¹) that was maintained until saturated adsorption was achieved. The system was purged with He to remove non-adsorbed CO and IR spectra were collected, such that CO adsorption data at 160 °C were obtained. After the treatment with He, the reactivity of adsorbed CO species (CO_{ad}) was monitored by switching to a 10 vol% H₂ in He flow (20 mL min⁻¹). Simultaneously, IR spectra were recorded every 30 s for 10 min. This experiment is referred to the reactivity of CO_{ad} at 160 °C.

Fischer–Tropsch tests. FTS trials were performed in a stainless-steel fixed-bed reactor with an inner diameter of 12 mm under high pressure. Typically, the Ru/TiO₂ catalyst (20–40 mesh, 0.3 g) was diluted with quartz sand (20–40 mesh, 0.9 g) and loaded into the reactor. Prior to each reaction, the catalyst was reduced in a H₂ gas flow (20 mL min⁻¹) at the desired temperature (200–600 °C) for 2 h. After the reactor was cooled down, a syngas with a H₂/CO ratio of 2/1 (H₂/CO/Ar = 64/32/4 (v/v/v)) was introduced into the reactor at a flow rate of 15 mL min⁻¹ (space velocity = 3000 mL g_{cat}⁻¹ h⁻¹). Ar was used as an internal standard to calculate CO conversion and selectivity of CH₄ and CO₂. The reaction was carried out at 160 °C under 2.0 MPa. After passing through a hot trap (120 °C) and then an ice-bath, the gaseous products were analyzed online using an Agilent 7890 gas chromatograph equipped with an HP-PLLOT/Q capillary column connected to a flame ionization detector (FID) and a TDX-01 column connected to a thermal conductivity detector (TCD). The data of the catalytic performances of Ru/TiO₂ catalysts were collected at the stable stage after at least 6 h of running. The calculation method for FTS catalytic performance was described in detail in the supplementary information.

SSITKA experiments. Steady-state isotopic transient kinetic analysis (SSITKA) is a combination of steady-state and transient techniques that can provide a reliable kinetic model to gain insights into the reaction mechanism. In this study, we used SSITKA to explore the activity of the Ru/TiO_{2-x} catalysts with the aim of providing insights into the intrinsic promotional effects. During each SSITKA experiment, 50 mg of the sieved catalyst mixed with 200 mg of SiC was pretreated in situ in a H₂/Ar flow (20/20 mL min⁻¹) at the desired temperature (300, 450, or 600 °C). After cooling to 100 °C, the feed was switched to a ¹²CO/Ar mixture (35 mL min⁻¹, 0.85 bar CO, 1.77 bar inert). CO adsorption was determined by switching from ¹²CO/Ar to ¹³CO/Kr without changing the other reaction conditions. Subsequently, the feed was switched to ¹²CO/H₂/Ar (1.5/15/33.5 mL min⁻¹, 1.85 bar) for CO hydrogenation at 200 °C. After 6 h on stream, a switch from ¹²CO/H₂/Ar to ¹³CO/H₂/Kr was employed to study isotopic transients, while maintaining the CO conversion at $\sim 10\%$. The isotopic transient response was determined by mass spectrometer.

The TOF values were calculated as

$$\text{TOF}_{\text{CO}} = \frac{R_{\text{CO}} \cdot M_{\text{Ru}}}{D \cdot x_{\text{Ru}}} \quad (1)$$

and

$$\text{TOF}_{\text{CH}_4} = \frac{R_{\text{CO}} \cdot S_{\text{CH}_4} \cdot M_{\text{Ru}}}{D \cdot x_{\text{Ru}}} \quad (2)$$

where R_{CO} is the CO consumption in moles per gram of catalyst, S_{CH_4} is the methane selectivity, M_{Ru} is the atomic mass of Ru, D is the Ru dispersion and x_{Ru} is the Ru loading of the sample.

The surface coverage of intermediates leading to CH₄ was calculated as

$$\theta_{\text{CH}_4} = \frac{N_{\text{CH}_4}}{N_{\text{Total}}} \quad (3)$$

where N_{CH_4} is the number of intermediates leading to methane and N_{Total} is the total number of active sites, as determined by the reversible adsorption of CO in the SSITKA experiments.

Computational details. Density functional theory (DFT) calculations were performed using the Vienna Ab-initio Simulation Package (VASP, a version of 5.4.4)^{40,41}. The Perdew–Burke–Ernzerhof (PBE) exchange–correlation functional was used to initial calculation⁴². The core and valence electrons were represented by the projector augmented wave (PAW) potential, and the plane wave basis set with a cut-off energy of 500 eV was used. A TiO_x cluster covered on a four-layered slab of the close-packed (001) surface derived from the hcp phase of Ru, was used as a model to the TiO_x overlayer covered Ru nanocatalyst. A vacuum gap of 15 Å was used to separate periodic images of the slab in the direction perpendicular to the surface. The atoms in the top two layers of Ru(001) were allowed to relax during optimization. The Brillouin zone of the 4 × 4 surface unit cell of Ru(001) was sampled with a 2 × 2 × 1 Monkhorst–Pack grid. Optimized geometries were obtained by minimizing the forces on the atoms below 0.02 eV Å⁻¹. The transition state was first isolated using the climbing image nudged elastic band (CI-NEB) method and then refined using the dimer method to until force is below 0.02 eV Å⁻¹⁴³. After that, the newly developed GW potential was adopted for the further optimization of adsorption geometries and transition states. The resulting transition state was finally confirmed by the normal mode frequency analysis, showing only one imaginary mode. We have first compared the relative stability of different TiO_x (x = 1–4) clusters on the Ru(001) surface under different reduction degree condition which can be represented as the variation of chemical potential of oxygen, and was calculated according to the procedure of previous research⁴⁴. In our calculation, the data of the formation energy of rutile TiO₂ was acquired from the reference⁴⁵. Other computational details are shown in the Supplementary Information.

Data availability

The data that support the findings of this study are available from the corresponding author upon reasonable request.

Received: 9 December 2019; Accepted: 2 June 2020;

Published online: 24 June 2020

References

- Zhong, L. et al. Cobalt carbide nanoprisms for direct production of lower olefins from syngas. *Nature* **538**, 84–87 (2016).
- Li, J. et al. Integrated tuneable synthesis of liquid fuels via Fischer–Tropsch technology. *Nat. Catal.* **1**, 787–793 (2018).
- Torres Galvis, H. M. et al. Supported iron nanoparticles as catalysts for sustainable production of lower olefins. *Science* **335**, 835–838 (2012).
- Torres Galvis, H. M. et al. Iron particle size effects for direct production of lower olefins from synthesis gas. *J. Am. Chem. Soc.* **134**, 16207–16215 (2012).
- Fischer, N., Clapham, B., Feltes, T. & Claeys, M. Cobalt-based Fischer–Tropsch activity and selectivity as a function of crystallite size and water partial pressure. *ACS Catal.* **5**, 113–121 (2015).
- Sun, J. et al. Highly-dispersed metallic Ru nanoparticles sputtered on H-beta zeolite for directly converting syngas to middle isoparaffins. *ACS Catal.* **4**, 1–8 (2014).
- Lighthart, D. A. J. M. et al. EJM. Identification of step-edge sites on Rh nanoparticles for facile CO dissociation. *Catal. Commun.* **77**, 5–8 (2016).
- Simonetti, D. A., Rass-Hansen, J., Kunkes, E. L., Soares, R. R. & Dumesic, J. A. Coupling of glycerol processing with Fischer–Tropsch synthesis for production of liquid fuels. *Green Chem.* **9**, 1073–1083 (2007).
- Carballo, J. M. G. et al. Catalytic effects of ruthenium particle size on the Fischer–Tropsch synthesis. *J. Catal.* **284**, 102–108 (2011).
- Kang, J., Deng, W., Zhang, Q. & Wang, Y. Ru particle size effect in Ru/CNT-catalyzed Fischer–Tropsch synthesis. *J. Energ. Chem.* **22**, 321–328 (2013).
- Kang, J., Zhang, S., Zhang, Q. & Wang, Y. Ruthenium nanoparticles supported on carbon nanotubes as efficient catalysts for selective conversion of synthesis gas to diesel fuel. *Angew. Chem. Int Ed.* **48**, 2565–2568 (2009).
- Ojeda, M. et al. CO activation pathways and the mechanism of Fischer–Tropsch synthesis. *J. Catal.* **272**, 287–297 (2010).
- Loveless, B. T., Buda, C., Neurock, M. & Iglesia, E. CO chemisorption and dissociation at high coverages during CO hydrogenation on Ru catalysts. *J. Am. Chem. Soc.* **135**, 6107–6121 (2013).
- González Carballo, J. M. et al. Support effects on the structure and performance of ruthenium catalysts for the Fischer–Tropsch synthesis. *Catal. Sci. Technol.* **1**, 1013–1023 (2011).
- Li, W. Z. et al. Chemical insights into the design and development of face-centered cubic ruthenium catalysts for Fischer–Tropsch synthesis. *J. Am. Chem. Soc.* **139**, 2267–2276 (2017).
- Tauster, S. J., Fung, S. C., Baker, R. T. K. & Horsley, J. A. Strong interactions in supported-metal catalysts. *Science* **211**, 1121–1125 (1981).

17. Tauster, S. J., Fung, S. C. & Garten, R. L. Strong metal-support interactions. Group 8 noble metals supported on titanium dioxide. *J. Am. Chem. Soc.* **100**, 170–175 (1978).
18. Komaya, T. et al. Effects of dispersion and metal-metal oxide interactions on Fischer-Tropsch synthesis over Ru/TiO₂ and TiO₂-promoted Ru/SiO₂. *J. Catal.* **150**, 400–406 (1994).
19. Xu, J. et al. Influence of pretreatment temperature on catalytic performance of rutile TiO₂-supported ruthenium catalyst in CO₂ methanation. *J. Catal.* **333**, 227–237 (2016).
20. Abdel-Mageed, A. M. et al. Selective CO methanation on Ru/TiO₂ catalysts: role and influence of metal-support interactions. *ACS Catal.* **5**, 6753–6763 (2015).
21. van Deelen, T. W., Hernández Mejía, C. & de Jong, K. P. Control of metal-support interactions in heterogeneous catalysts to enhance activity and selectivity. *Nat. Catal.* **2**, 955–970 (2019).
22. Kikuchi, E., Matsumoto, M., Takahashi, T., Machino, A. & Morita, Y. Fischer-Tropsch synthesis over titania-supported ruthenium catalysts. *Appl. Catal.* **10**, 251–260 (1984).
23. Hernandez Mejia, C., van Deelen, T. W. & de Jong, K. P. Activity enhancement of cobalt catalysts by tuning metal-support interactions. *Nat. Commun.* **9**, 4459–4466 (2018).
24. Lin, Q. et al. Crystal phase effects on the structure and performance of ruthenium nanoparticles for CO₂ hydrogenation. *Catal. Sci. Technol.* **4**, 2058–2063 (2014).
25. Badyal, J. P. S. & Lambert, R. M. Surface oxide films and H₂/CO chemisorption at the Ru/TiO₂ interface: studies with a model planar catalyst. *J. Catal.* **130**, 173–180 (1991).
26. Green, C. L. & Kucernak, A. Determination of the platinum and ruthenium surface areas in platinum-ruthenium alloy electrocatalysts by underpotential deposition of copper. I. Unsupported catalysts. *J. Phys. Chem. B* **106**, 1036–1047 (2002).
27. Yang, J. et al. Reaction mechanism of CO activation and methane formation on Co Fischer-Tropsch catalyst: a combined DFT, transient, and steady-state kinetic modeling. *J. Catal.* **308**, 37–49 (2013).
28. Ledesma, C., Yang, J., Chen, D. & Holmen, A. Recent approaches in mechanistic and kinetic studies of catalytic reactions using SSITKA technique. *ACS Catal.* **4**, 4527–4547 (2014).
29. Lohitharn, N. & Goodwinjr, J. Impact of Cr, Mn and Zr addition on Fe Fischer-Tropsch synthesis catalysis: investigation at the active site level using SSITKA. *J. Catal.* **257**, 142–151 (2008).
30. Hadjivanov, K. et al. FTIR study of CO interaction with Ru/TiO₂ catalysts. *J. Catal.* **176**, 415–425 (1998).
31. González-Carballo, J. M. et al. In-situ study of the promotional effect of chlorine on the Fischer-Tropsch synthesis with Ru/Al₂O₃. *J. Catal.* **332**, 177–186 (2015).
32. Elmasides, C., Kondarides, D. I., Grünert, W. & Verykios, X. E. X. P. S. and FTIR study of Ru/Al₂O₃ and Ru/TiO₂ catalysts: reduction characteristics and interaction with a methane-oxygen mixture. *J. Phys. Chem. B* **103**, 5227–5239 (1999).
33. Robbins, J. L. Chemistry of supported Ru: CO-induced oxidation of Ru at 310 K. *J. Catal.* **115**, 120–131 (1989).
34. Solymosi, F. & Raskó, J. An infrared study of the influence of CO adsorption on the topology of supported ruthenium. *J. Catal.* **115**, 107–119 (1989).
35. Gupta, N. M. et al. FTIR spectroscopic study of the interaction of CO₂ and CO₂ + H₂ over partially oxidized Ru/TiO₂ catalyst. *J. Catal.* **146**, 173–184 (1994).
36. Johnson, G. R., Werner, S. & Bell, A. T. An investigation into the effects of Mn promotion on the activity and selectivity of Co/SiO₂ for Fischer-Tropsch synthesis: evidence for enhanced CO adsorption and dissociation. *ACS Catal.* **5**, 5888–5903 (2015).
37. Shetty, S. & van Santen, R. A. CO dissociation on Ru and Co surfaces: the initial step in the Fischer-Tropsch synthesis. *Catal. Today* **171**, 168–173 (2011).
38. Ciobica, I. M. & van Santen, R. A. Carbon monoxide dissociation on planar and stepped Ru(0001) surfaces. *J. Phys. Chem. B* **107**, 3808–3812 (2003).
39. Pilot, I. A., van Santen, R. A. & Hensen, E. J. The optimally performing Fischer-Tropsch catalyst. *Angew. Chem. Int. Ed.* **53**, 12746–12750 (2014).
40. Kresse, G. & Furthmüller, J. Efficient iterative schemes for ab initio total-energy calculations using a plane-wave basis set. *Phys. Rev. B* **54**, 11169–11186 (1996).
41. Kresse, G. & Joubert, D. From ultrasoft pseudopotentials to the projector augmented-wave method. *Phys. Rev. B* **59**, 1758–1775 (1999).
42. Perdew, J. P., Burke, K. & Ernzerhof, M. Generalized gradient approximation made simple. *Phys. Rev. Lett.* **77**, 3865–3868 (1996).
43. Henkelman, G., Uberuaga, B. P. & Jónsson, H. A climbing image nudged elastic band method for finding saddle points and minimum energy paths. *J. Chem. Phys.* **113**, 9901–9904 (2000).
44. Reuter, K. & Scheffler, M. Composition, structure, and stability of RuO₂(110) as a function of oxygen pressure. *Phys. Rev. B* **65**, 035406 (2001).
45. Lide, D. R. *CRC Handbook of Chemistry and Physics*, 88th edn (Taylor & Francis Group, Boca Raton, 2007).

Acknowledgements

This work was supported by the National Key R&D Program of China (2016YFA0202804), the Strategic Priority Research Program of the Chinese Academy of Sciences (XDB36030200), the National Natural Science Foundation of China (21978286, 21925803, 21776269), the Youth Innovation Promotion Association CAS.

Author contributions

Y.Z., X.F.Y., X.S., and Y.H. conceived and designed the project. Y.Z. performed the experiments. X.F.Y. carried out the theoretical calculations. X.L.Y. and D.C. finished the SSITKA experiments. H.Q. performed the X-ray absorption experiments. Y.S. conducted the TEM observations. H.D., B.L.L., H.T., and B.L. contributed to the structure characterizations. Y.Z., X.F.Y., X.S., Y.H., and T.Z. analyzed the experimental data and prepared the paper. All authors reviewed and contributed to the paper.

Competing interests

The authors declare no competing interests.

Additional information

Supplementary information is available for this paper at <https://doi.org/10.1038/s41467-020-17044-4>.

Correspondence and requests for materials should be addressed to X.Y., X.S. or Y.H.

Peer review information *Nature Communications* thanks Doan Pham Minh and the other, anonymous, reviewer(s) for their contribution to the peer review of this work. Peer reviewer reports are available.

Reprints and permission information is available at <http://www.nature.com/reprints>

Publisher's note Springer Nature remains neutral with regard to jurisdictional claims in published maps and institutional affiliations.



Open Access This article is licensed under a Creative Commons

Attribution 4.0 International License, which permits use, sharing, adaptation, distribution and reproduction in any medium or format, as long as you give appropriate credit to the original author(s) and the source, provide a link to the Creative Commons license, and indicate if changes were made. The images or other third party material in this article are included in the article's Creative Commons license, unless indicated otherwise in a credit line to the material. If material is not included in the article's Creative Commons license and your intended use is not permitted by statutory regulation or exceeds the permitted use, you will need to obtain permission directly from the copyright holder. To view a copy of this license, visit <http://creativecommons.org/licenses/by/4.0/>.

© The Author(s) 2020